Implantable Multifunctional Bioresorbable Optics

Authors: Hu Tao[1,‡], Jana M. Kainerstorfer[1,‡], Sean M. Siebert[1], Eleanor M. Pritchard[1], Angelo Sassaroli[1], Bruce J. B. Panilaitis[1], Mark A. Brenckle[1], Jason J. Amsden[1], Jonathan Levitt[2], Sergio Fantini[1], David L. Kaplan[1,3], and Fiorenzo G. Omenetto[1,4,*]

Affiliations:
[1]Department of Biomedical Engineering, Tufts University 4 Colby St., Medford, MA.
[2]Department of Physics of Complex Systems, Weizmann Institute of Science, Rehovot, Israel
[3]Department of Chemical & Biological Engineering Tufts University 4 Colby St., Medford, MA.
[4]Department of Physics & Astronomy Tufts University 4 Colby St., Medford, MA.
*fiorenzo.omenetto@tufts.edu
[‡]contributed equally to this work

Supplementary Materials:
Figures S1-S24
Table T1
References (*30-39*)
Materials and Methods

Supplementary Materials:

Device fabrication

Silk can be easily formed into mechanically robust films of thermodynamically-stable beta sheets, with control of thicknesses and surface feature sizes from just below ten nanometers to hundreds of micrometers or more. These films are formed by simple casting of purified silk solution which crystallizes upon exposure to air, without the need for exogenous cross-linking reactions or post processing cross-linking for stabilization.

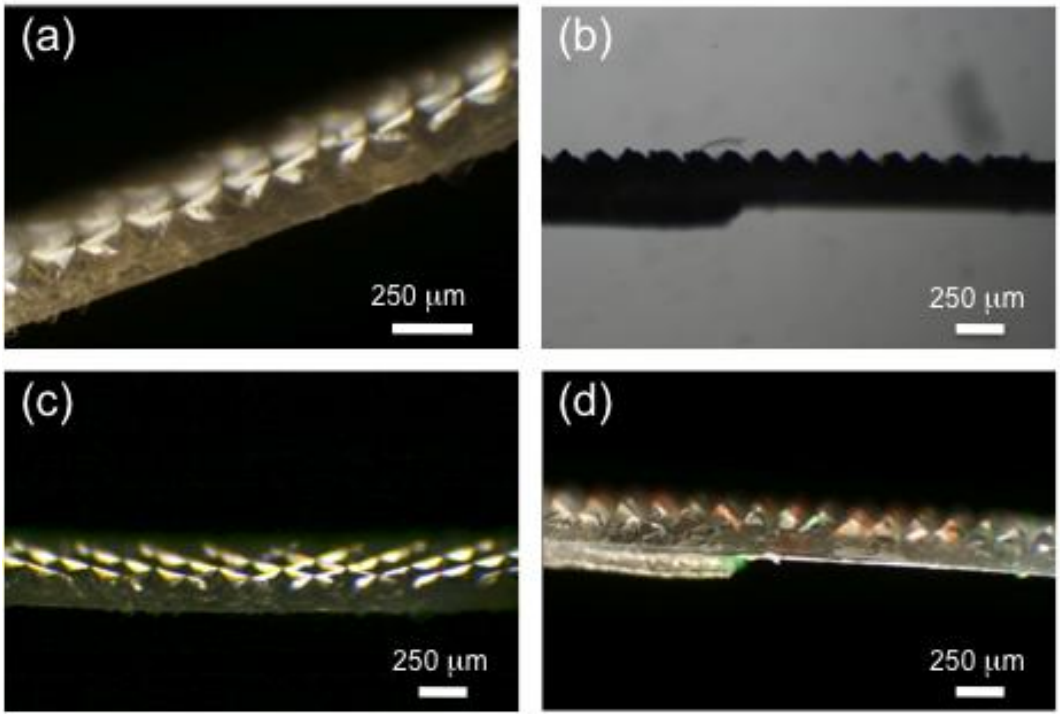

Figure S1. Microscopy images of the silk micro-prism reflectors used for the implants.

A water-based silk fibroin solution was obtained by extraction and purification of harvested *Bombyx mori* cocoons. This previously described process yields an 6.5-8 %w/v silk fibroin solution which is then cast onto a microprism master mould (3M Scotchlite™ Reflective Material – High Gloss Film). The master consists of an array of microprisms with dimensions of roughly 100 micrometers and clustered in groups as shown in Figure S1 & S2. The silk is dried for 8-12 hours upon which it is mechanically detached from the master surface. Upon microscopic examination, the silk retroreflective films replicates the master and have a reflective appearance similar to the master mould. The index of refraction of silk is n=1.54

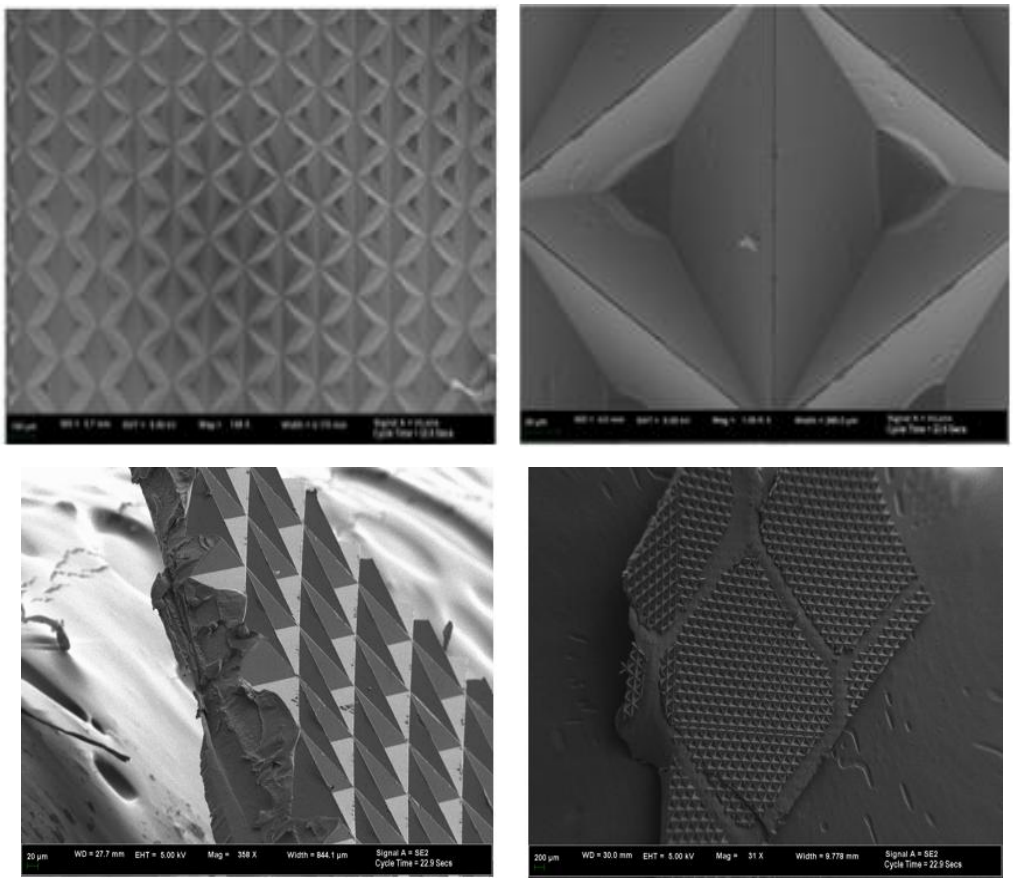

Figure S2 – SEM images of silk MPAs

The dissolution rate of silk films is readily and controllably tunable, from instantaneous to years, via variation of the degree of crystallinity (β sheet content) introduced during material processing as shown in figure S3A.[from Hu X, et al., "Microphase separation controlled beta-Sheet crystallization kinetics in fibrous proteins," Macromolecules 2009; 42:2079 2087]. This offers the possibility of creating structures and devices thatare programmably degradable. Silk dissolution itself is mediated by chemical and biochemical processes such as enzymatic degradation.

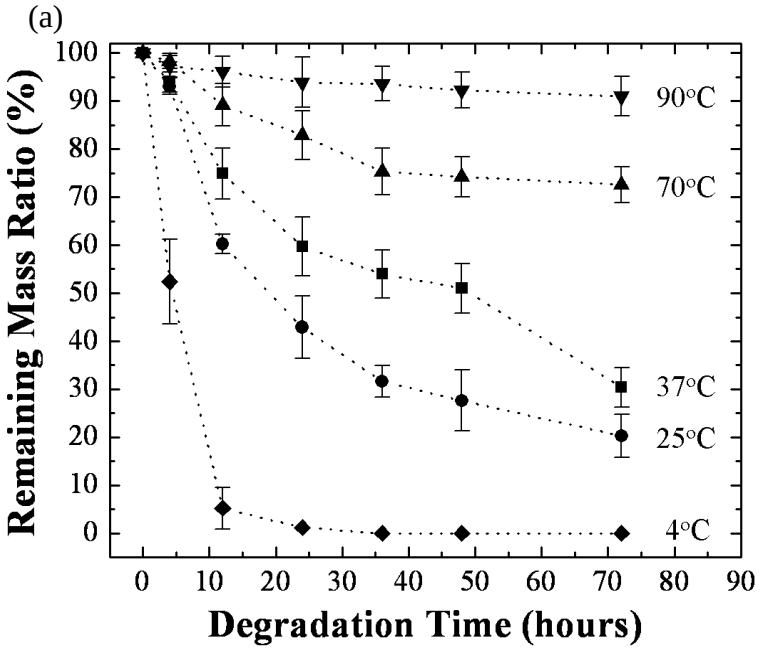

Figure S3 - (A) Enzymatic degradation of silk films by protease XIV under standard reaction conditions at 37°C. The temperatures on the right side of the Figure indicate the temperatures used to anneal the films to control crystalline content [4°C, 25°C, 37°C, 70°C, 95°C].

Silk MPA characterization and baseline evaluation in the presence of scattering media

The silk reflector replicated the master faithfully and its optical performance matched the master's, providing orders of magnitude of measured increase in the diffuse reflection when compared to the background without any reflective surface (Figure S4). For the device to be adaptable to biomedical environments, it must successfully integrate and operate in humid or wet scattering environments. Performance of the silk MPAs under these conditions was assessed by placing the silk reflector films under a 4 cm thick block of gelatin or submerged in a talcum powder and water suspension at a depth of 6.5 cm. In both cases the presence of the reflector resulted in a significant enhancement of signal at the detector plane, increasing the backscattered signal intensity in both cases and allowing easy imaging (with a commercial CCD camera) of the reflector under isotropic illumination (Figure S5).

It must be noted that, in contrast to the *in-vivo* and part of the *in-vitro* measurements, these baseline measurements are performed using the fiber probe at a distance from the scattering surface and not in contact with the scattering surface (in contrast, for example, with the *in vivo* and deep tissue experiments where the fiber probe is placed in contact with the skin)

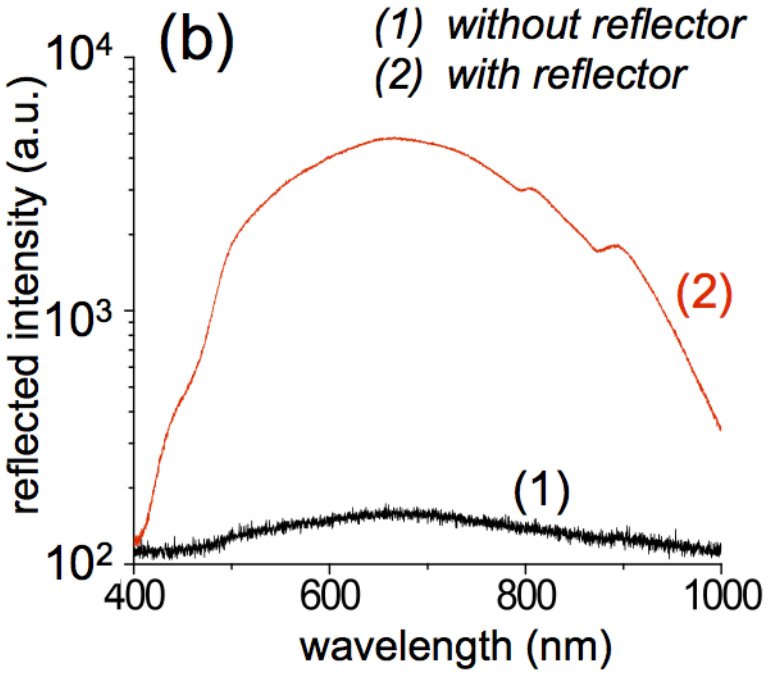

Figure S4. The silk micro-prism reflector shows several orders of magnitude increase in reflected signal compared to the background signal in open air when the signal is collected at a distance from the sample. (1) is the reflected background from a diffusing surface whereas (2) is the reflected signal at the same distance with a microprism located onto the diffusing surface.

Commonly used for safety applications, the performance of retroreflecting films is defined by measuring the luminous intensity and retroreflector coefficients per illuminance level on the surface of the retroreflector (in candelas/lx and candelas/(lx/m^2), respectively). Designed for broad angle reflection in safety clothing and garments, the films have a reflection coefficient (defined as the ratio of the coefficient of luminous intensity of a plane retroreflecting surface to its area expressed in candelas per square meter) between 300 and 400.

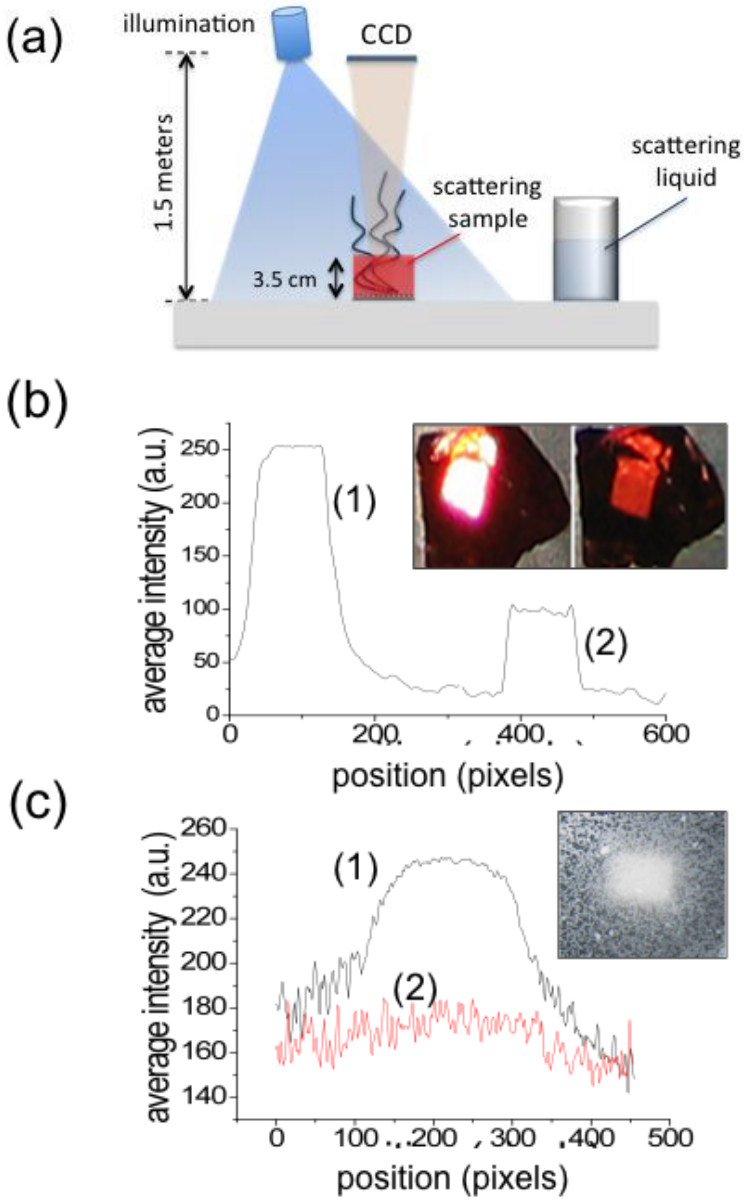

Figure S5. Schematic setup and images of silk micro-prism reflectors embedded in scattering media. The system was exposed to isotropic illumination from a white light source - the reflection from the films was collected at a distance of 1.5 meters with a digital CCD camera as illustrated in (A). Figure (B) shows images of the silk reflector and a flat substrate under 3.5 cm of gelatin and the corresponding lineout extracted from the image. Figure (Cc) shows the image acquired from the CCD when the silk reflector was immersed under 6.5 cm of scattering solution composed of talcum and water. The silk reflector was attached to the bottom of a dark container and then covered with the solution.

Performance characterization in biological tissues – superficial imaging

While the previous results establish a necessary baseline, in an optical diagnostic situation involving light scattering, it is important to acquire specific spectral information from the volume under test to associate it with physiological markers of interest.

With this premise, two spectrally responsive elements embedded in biological tissue were used and an in-vitro experiment was performed to assess the variation in the optical response when the device was present. The silk reflector was placed underneath two types of spectral filters: a 10 nm bandpass multilayer filter (with central wavelength λ_0 = 630 nm) and a layer of cellulose embedded with red pigment. These were chosen to provide known broadband and narrowband spectral responses to embed in tissue constructs to test the efficacy of the device. The reflector/spectral element was then covered either by single or multiple layers of 800-micrometer thick porcine fat or muscle tissue (Figure 1). The resulting structure was then probed by illumination with incoherent white light delivered through a multimode fiber. The latter is part of a fiber-backscattering probe which acts as the collector for the diffuse retroreflected scattering signal and redirects it to a spectrometer.

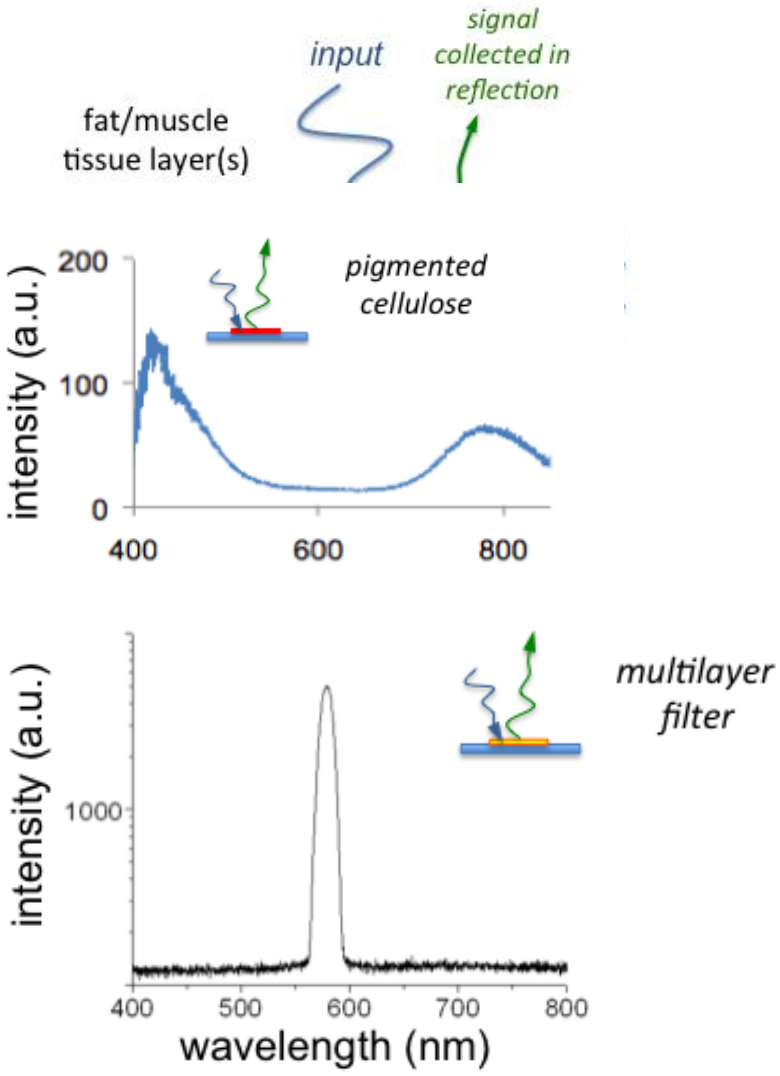

Figure S6. Spectral response of both the pigmented cellulose layer and the multilayered spectral filter used in the experiments. The layout of the experiment is illustrated at the top and serves as the basis for the layout of the in-vitro experiment.

Baseline response from porcine muscle tissue.

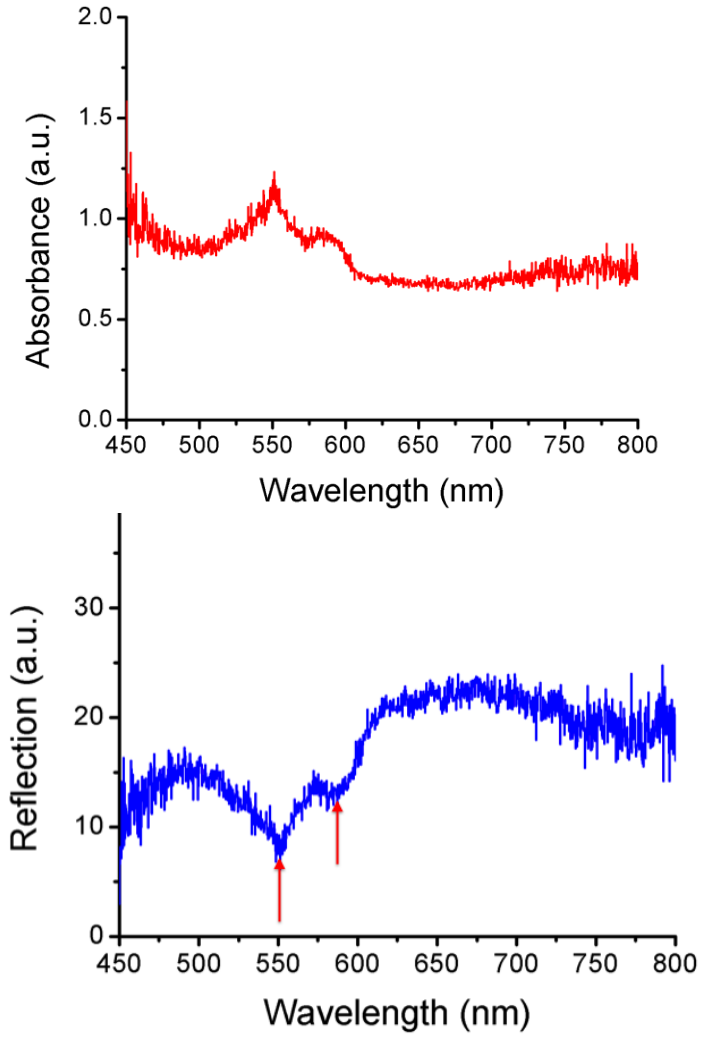

Figure S7. Results from in-vitro experiments measuring the baseline absorbance and corresponding reflection of a single layer of porcine muscle tissue. Two absorption features are detectable at wavelengths of ~550 nm and ~575 nm. These features are apparent in the MPA enhanced measurement described in the main text.

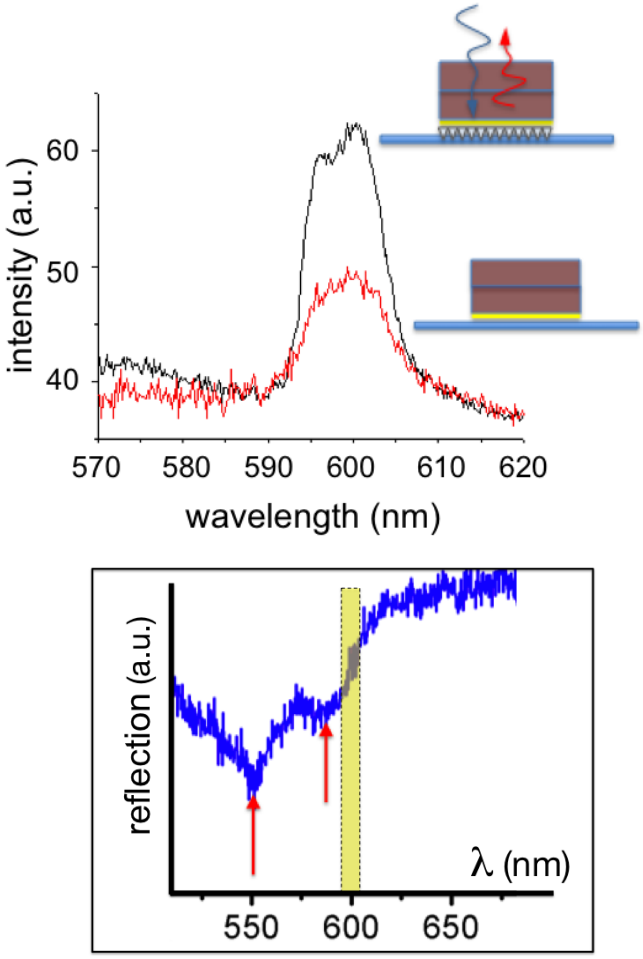

Figure S8. (b) Results from in-vitro experiments with incoherent illumination and detection through a fiber probe of the backscattered spectrum through porcine muscle tissue layers in the presence of a multilayer (λ=600 nm, $\Delta\lambda$~10 nm) dielectric notch filter and resulting enhancement of the detected response with the addition of a silk micro-prism array. The figure also shows the bandwidth of the dielectric notch filter superimposed on the reflection baseline measurement shown earlier in Figure S7

Performance characterization in biological tissues – deep tissue imaging

In order to evaluate the performance on deep tissue, experiments on solid Delrin phantoms, which are highly scattering and mimic well the scattering in tissue, and liquid phantoms, which were made of a milk, water, and ink mixture, mimicking not only scattering, but absorption in tissue. The Delrin phantom had a given thickness of 10mm, the thickness of the liquid phantom was varied between 2mm and 10mm. The geometry of the imaging setup was such that a broadband (white) light source (halogen) was used for illumination and a detection fiber was scanned over the tissue, leading to source – detector positions between 8mm and 38mm, in 2mm increments. The reflected signal was collected in a spectrometer setup (Model SP-150, Acton Research Corp., Acton, Massachusetts). This scanning geometry was chosen in order to evaluate the spatial dependence of signal enhancement and also because it is well known that deeper, highly scattering tissue can only be imaged when there is a certain distance between the source and detector, where the distance is depth dependent[30-34]. Imaging was performed on the phantoms for four different scenarios – Phantom alone, mirror embedded at the depth of interest, a 8mm x 8mm neutral density (ND) filter (OD=0.6) piece on top of the mirror, and the ND without the mirror. The ND piece was used to mimic a local inclusion for evaluating the contrast enhancement. The location of the ND filter was ~16mm away from the source fiber in the x-y plane.

Signal enhancement

Signal enhancement was evaluated by imaging the phantom with and without the embedded mirror. The ratio between those two gives the enhancement in reflected intensity, hence signal enhancement. In the case of the solid phantom, where the mirror is embedded at 10mm depth, we found that the signal could be enhanced 1.45 times in comparison to not having the mirror. This is a 45% enhancement at 10mm depth of a highly scattering medium. For the liquid phantom without milk, a 1.25 times enhancement could be found. For the liquid phantom, where ink was used for mimicking absorption, a 15-20% enhancement could still be found at 10mm depth. For shallower depths, this enhancement is even larger.

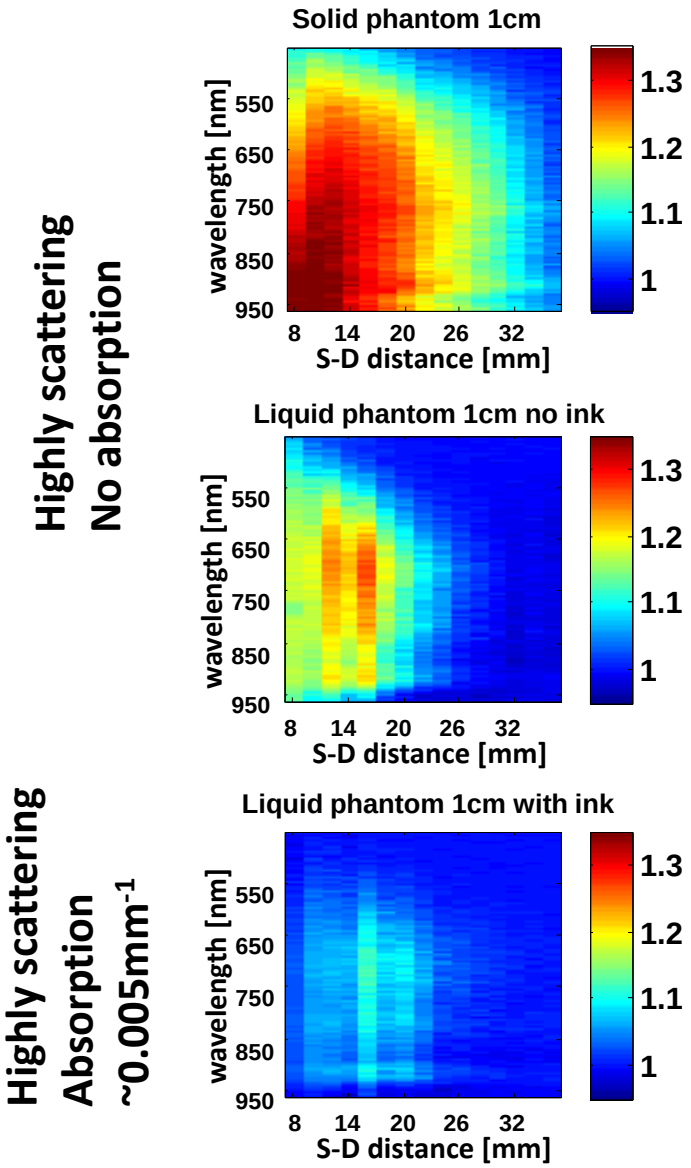

Figure S9. Results from in-vitro deep tissue experiments. The MPA shows significant increase in reflected signal compared to measuring reflectance from the phantom alone. This increase in signal is slightly reduced in the liquid phantom (without ink) and further reduced with ink as an absorbing material. A 15-20% enhancement could still be found at 10mm depth in the liquid absorbing phantom.

Contrast enhancement

Optical imaging of malignancies has two major challenges – accessibility and contrast to healthy surrounding tissue. If the malignancy is too deep to be imaged, information content is lost. This limitation has been addressed in the previous paragraph, where we show that the signal can be enhanced even in 10mm depth. The maybe even more important question is if contrast can be enhanced. For answering this question, we used a small piece of ND filter, mimicking an inclusion in tissue.

Contrast was defined as (I-I0)/I0, where I is the intensity measured with the ND being present and I0 without the ND filter (background signal). In the case of having the mirror embedded, I0 is the intensity reflected from the phantom with the mirror; in the case of no mirror, I0 is the intensity measured on the phantom alone.

For the solid phantom, having the ND inclusion at 10mm depth, we were able to see a ~3 times bigger contrast with the mirror being present in comparison to not having the mirror. In the case of the liquid phantom without ink, a 3 times bigger contrast, and with ink a ~1.5 times bigger contrast was found, hence a 50% increase in contrast when the mirror is present.

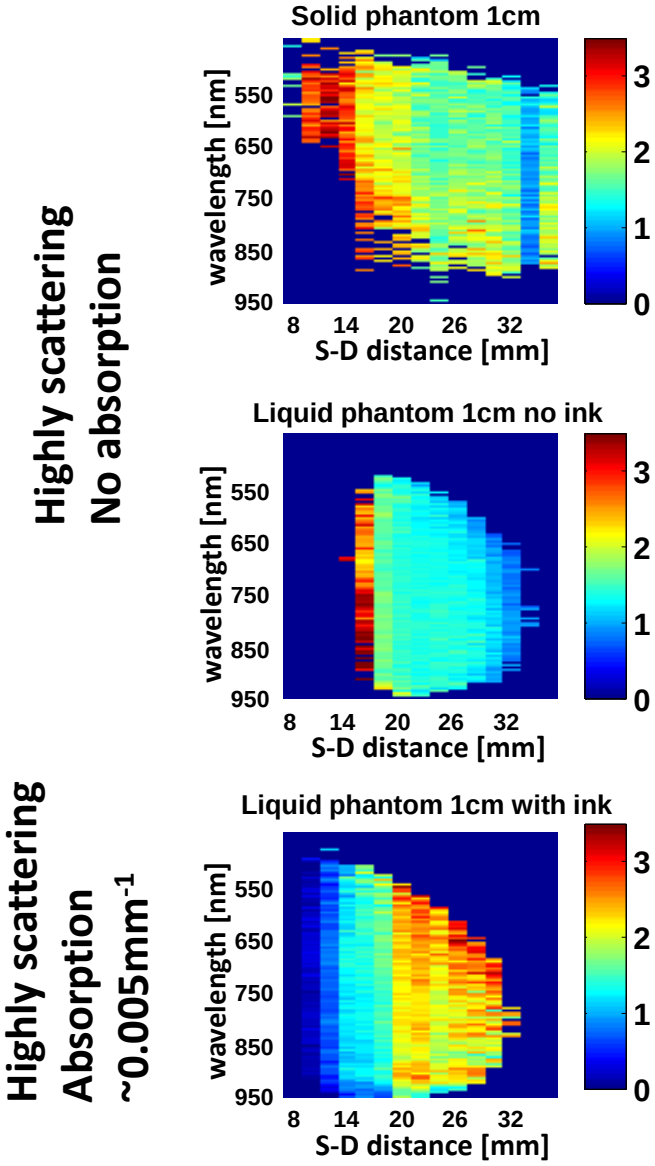

Figure S10. Results from in-vitro deep tissue experiments. The contrast enhancement for measuring the ND filter is increased 3.5 times at source detector distance of 12mm and is still 3 times for the liquid phantom without ink. The contrast increase in the absorbing liquid phantom was 1.5 times at the same source detector distance and even bigger for larger source detector distances.

30. Arridge, S.R. & Schweiger, M. Photon-measurement density functions. Part 2: Finite-element-method calculations. Appl Opt 34, 8026-8037 (1995).
31. Arridge, S.R. Photon-measurement density functions. Part I: Analytical forms. Appl Opt 34, 7395-7409 (1995).
32. Del Bianco S, Martelli F, Zaccanti G, Penetration depth of light re-emitted by a diffusive medium: theoretical and experimental investigation. Phys Med Biol. 47(23):4131-44 (2002).
33. Michael S. Patterson, Stefan Andersson-Engels, Brian C. Wilson, and Ernest K. Osei, "Absorption spectroscopy in tissue-simulating materials: a theoretical and experimental study of photon paths," Appl. Opt. 34, 22-30 (1995)
34. R. F. Bonner, R. Nossal, S. Havlin, and G. H. Weiss, "Model for photon migration in turbid biological media," J. Opt. Soc. Am. A 4, 423-432 (1987)

In-vivo experiments: Reflectivity spectra of undoped plain silk film and micro-prism reflectors at 0 week and 2 weeks (N=3)

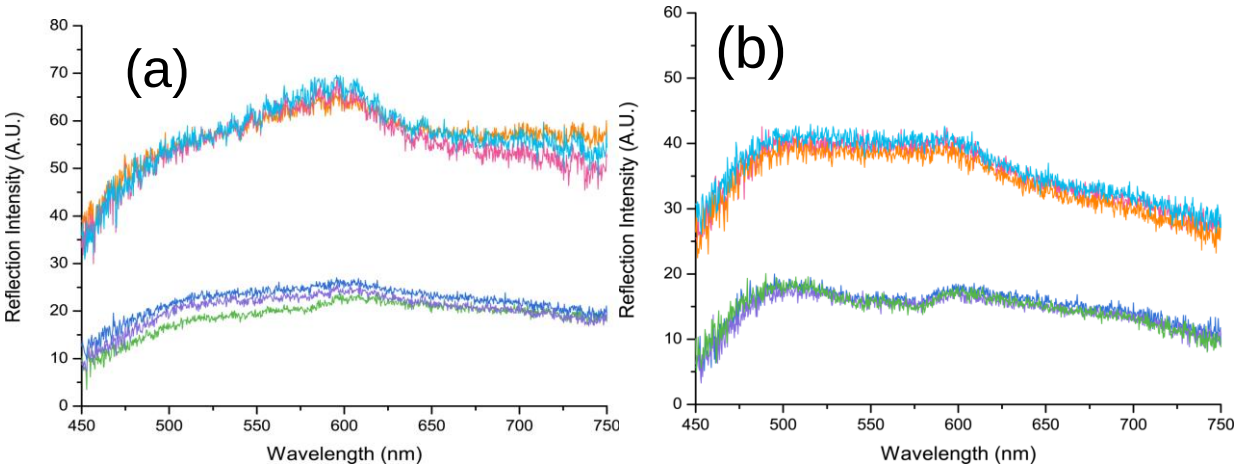

Figure S11. Reflectivity spectra of undoped micro-prism film and plain silk at (A) 0 week and (B) 2 weeks (N=3). The optical fiber probe was placed against the mouse skin for the reflectivity measurements. The integration time was 25 millisecond with data average number = 10.

In-vivo experiments: Reflectivity spectra of micro-prism film, plain film and mouse skin.

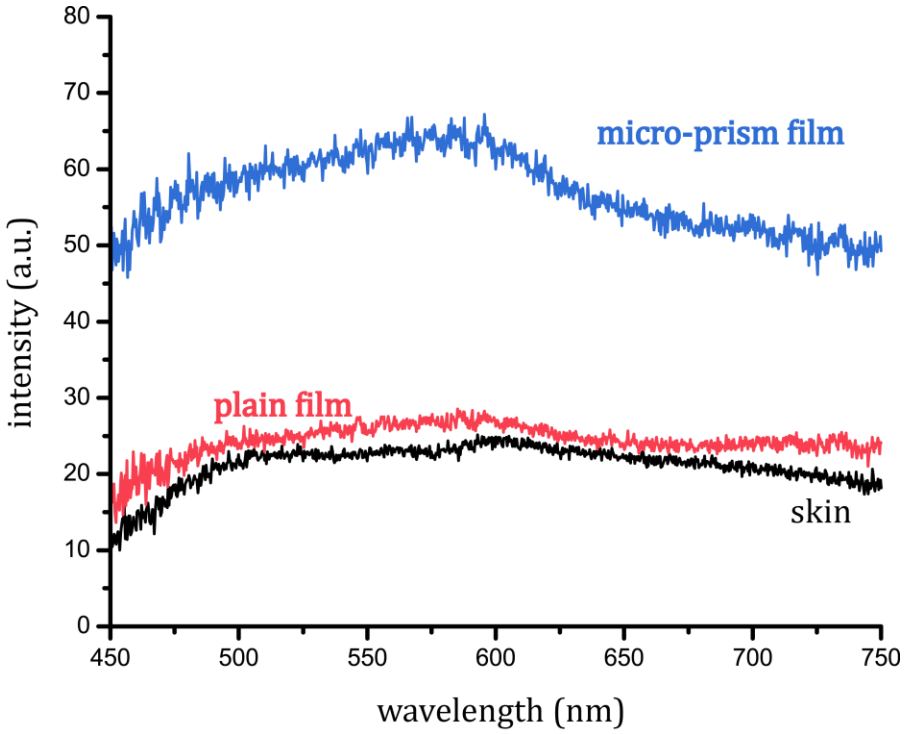

Figure S12. Reflectivity spectra of micro-prism film, plain silk and bare mouse skin. The optical fiber probe was placed against the mouse skin for the reflectivity measurements. The optical fiber probe was placed against the mouse skin for the reflectivity measurements. The integration time was 25 millisecond with data average number = 10.

Modeling

a) **The Radiative Transfer Equation**

The Radiative Transfer Equation (RTE) is written as:

$$\frac{1}{v}\frac{\partial I(\vec{r},\hat{s},t)}{\partial t}+\hat{s}\cdot\vec{\nabla}I(\vec{r},\hat{s},t)+\mu_t I(\vec{r},\hat{s},t)=\mu_s\int_{4\pi}p(\hat{s},\hat{s}')I(\vec{r},\hat{s}',t)d\Omega'+S(\vec{r},\hat{s},t) \qquad (1)$$

The RTE is an integro-differential equation that is widely used for describing light propagation in random media (as biological tissues)[35]. It is derived from general principles of energy balance at a microscopic level.

In Eq.(1) the meaning of the symbols is:

$I(\vec{r},\hat{s},t)$ is the specific intensity (or Irradiance) which is the number of photons per unit area, unit time and unit solid angle, which are found at time *t* in the position $\vec{r}$ around the direction $\hat{s}$;

v is the speed of light in the medium;

μ_s and μ_t are the scattering and total extinction coefficient, respectively, where $\mu_t = \mu_s + \mu_a$, and μ_a is the absorption coefficient;

$p(\hat{s},\hat{s}')$ is the phase function, which represents the probability density per unit solid angle that a photon traveling along $\hat{s}'$ is scattered along $\hat{s}$; the phase function is assumed to depend only on the product $\hat{s}'\cdot\hat{s}$ (scattering angle θ);

$S(\vec{r},\hat{s},t)$ is a source term, that is the number of photons, per unit time, unit volume and unit solid angle that are generated at time *t* in the point $\vec{r}$ around the direction $\hat{s}$.

In Eq.(1) it is assumed that only photons in a narrow frequency band are traveling in the medium (i.e. scattering must be elastic). Eq.(1) is written in scalar form (which is the form used in this work), however it can be written also in vectorial form to describe propagation of polarized or partially polarized light. In this case the specific intensity must be replaced by a vector which components are the Stokes parameters[35].

b) **The Monte Carlo Method**

In order to describe the experimental results we have used a Monte Carlo code for solving the RTE. Monte Carlo is a stochastic method which solves Eq.(1) by direct simulation of the actual propagation of photons in random media according to well established statistical laws[36]. The core of MC code is a subroutine for the extraction of random numbers uniformly distributed in the interval (0, 1). By using a triplet of random numbers (w_1, w_2, w_3) we can update in the 3D space the location of a scattering event once the coordinates of the previous scattering event are known. It is assumed that the trajectory between two consecutive scattering events is a segment of straight line. Arbitrarily we can use the random number w_1 to define the path length *L* between the scattering events and w_2, w_3 to define the azimuthal and the scattering angle ϕ and θ respectively. The path length and the direction of the free flight between two consecutive scattering events are defined by the equalities:

$$L=-\frac{1}{\mu_s}ln(w_1);\quad \phi = 2\pi w_2;\quad w_3=2\pi\int_0^{\theta}p(\theta')sin(\theta')d\theta' \qquad (2)$$

The last equality of Eq.(2) (where $\theta' = \hat{s}'\cdot\hat{s}$) should be inverted (i.e. we have to find θ (w_3)) by resorting to numerical methods. Starting from the coordinates of the point where the photons are injected into the medium we can calculate the coordinates of each scattering event while the photon is moving in the medium. This procedure is repeated until the photon's

trajectory either intersects a specified area at the boundary of the medium where one or more detectors are located (useful or detected photon) or escapes from the medium (lost photon). Whenever the photon's trajectory intersects the boundary of the medium we can also take into account of reflections due to the refractive index mismatch between diffusing and surrounding medium. This is done by comparison of a newly extracted random number (w_4) with the reflection coefficient of unpolarized radiation (r_t) [37]:

$$r_t = \frac{1}{2}\left\{\left[\frac{tg(\theta_i - \theta_t)}{tg(\theta_i + \theta_t)}\right]^2 + \left[\frac{sin(\theta_t - \theta_i)}{sin(\theta_t + \theta_i)}\right]^2\right\} \qquad (3)$$

In Eq.(3) θ_t and θ_i are the transmitted and incident angle respectively calculated with respect to a direction perpendicular to the boundary at the point of intersection. If $w_4 < r_{tot}$ the photon is reflected and the new direction is calculated according to the formula $\theta_r = \theta_i$, where θ_r is the angle of reflection; if $w_4 > r_{tot}$ the photon exits the medium and the trajectory is terminated. By using the same method we can also consider discontinuities in the refractive index within the random medium. Here we have described the statistical rules (Eq. 2) of the so-called "White Monte Carlo", which is run for the case of a non-absorbing medium. The effect of the absorption coefficient is considered afterwards through the microscopic Beer-Lambert law: if a photon is detected after having traveled a total pathlength *l* through a non-absorbing medium, the probability to detect the same photon when the medium is absorbing is: $\exp(-\mu_a l)$. Therefore the effect of absorption is considered through re-scaling the weights of collected photons according to their pathlengths. One last note is about the phase function. Even though many choices are possible, when we study light propagation in biological tissues the Henyey-Greenstein (HG) phase function is widely adopted:

$$p(\theta) = \frac{1}{4\pi} \cdot \frac{1 - g^2}{[1 + g^2 - 2g\cos(\theta)]^{3/2}} \qquad (4)$$

In Eq.(4) "g" is the asymmetry parameter: $g = \langle\cos(\theta)\rangle$ which in biological tissue usually has a value larger than 0.8 (high probability of forward scattering). The phase function is normalized to "1" over the entire solid angle (4π steradians). More details on the Monte Carlo method can be found in references[38-39].

c) **Description of the results**

The reflectivity in presence of the microarray is compared to the "baseline" reflectivity found in tissue alone.

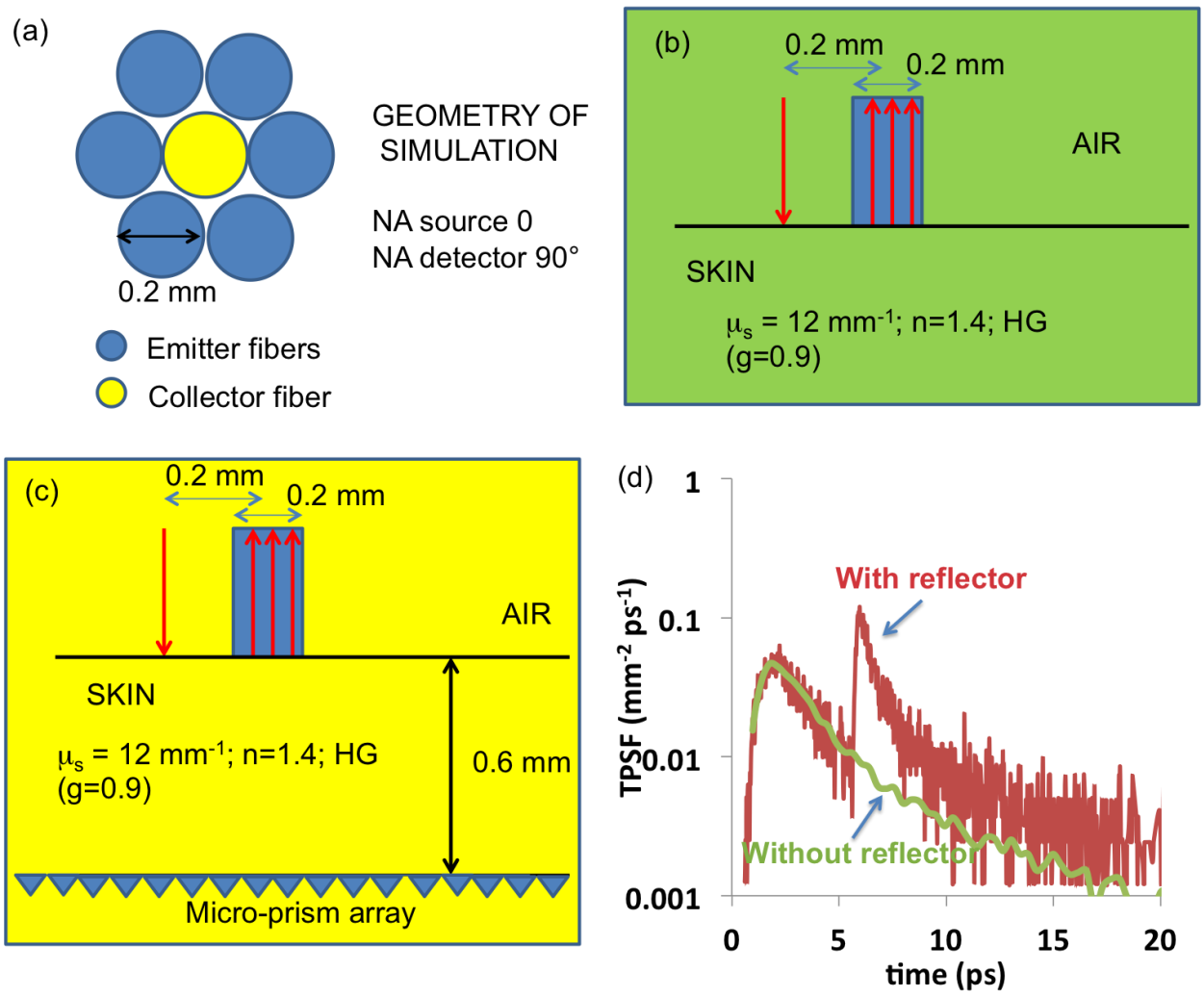

Figure S13. (A) Schematic of the geometry used for the simulation. The simulation models for the reflectivity (B) without reflectors and (C) with reflectors. (D) Comparison of temporal point spread function (TPSF) in the situations with and without reflector. Note that the peak of the maroon curve - i.e. with reflector - occurs around 6 ps, which is the "round trip" time for a photon to hit the microarray cube and be detected. The green curve – i.e. without reflector - is obtained in the tissue without microarray. It has been smoothed for display. Note that both curves share the same peak (very broad) around 2 ps, which is due to those photons that are detected without being reflected by the microarray. The speed of light in the tissue is assumed v= 0.214 mm/ps.

In this case, the Monte Carlo (MC) code that solves the time domain Radiative Transfer Equation (RTE see appendix) for a Dirac δ pulse as a source was used. More precisely the source (red pencil beam in Fig. S8) is: $\delta(\boldsymbol{r}-\boldsymbol{r_0})\delta(t-t_0)\delta(\hat{s}-\hat{s}_0)$, where $\boldsymbol{r}_0$ is the impinging point, t_0 is the injection time and $\hat{s}_0$ the impinging direction. MC calculates the temporal point spread function (TPSF) at the detector site. The TPSF is defined as the number of photons detected per unit time and area of the detector, normalized to the total number of injected photons. It is usually expressed in the units: mm^{-2} ps^{-1}. The reflectance is defined as the time-integral of the TPSF.

Total reflection was assumed at the skin-microarray boundary. The outcome of the simulations depends on a number of parameters. Some of these parameters affect in a negligible way the results like:

a) The model of Phase function. We chose the Heney-Greenstein phase function (HG), with asymmetry parameter g=0.9, which is typically used for biological tissues;

b) The exact model geometry of the source (cylindrical beam instead of point beam). We chose point beam;

c) The numerical aperture (NA) of the source and detector fibers. We chose 0 and 90°, respectively.

c) The absorption coefficient (which we varied in a very large range: between (0.01-0.2) mm^{-1}); we chose μ_a =0.01 mm^{-1} for the result in Fig. S13. This value is typical of bulk tissue, while 0.2 - 0.4 mm^{-1} is typical of blood.

If we change these parameters within reasonable ranges expected for tissue, we can change the reflectivity "R" of both situations [with (R1) or without (R0) microarray] by 10-20%, however the ratio of reflectivity for both situations R1/R0 changes by a much smaller amount (2-3 % at maximum). The ratio R1/R0 is affected minimally also by the choice of NA.

On the contrary the outcome of the simulations depends dramatically upon the choice of the scattering coefficient (μ_s) of the medium and the distance (d) between microarray and tissue surface. We found several combinations of these two parameters that yield a ratio R1/R0 in the order of the experimental one (~3). **The best choice of parameters was: μ_s = 12 mm^{-1}, d=0.6 mm.** Both values are very reasonable for tissue optical properties and location of the microarray, respectively, and yield the value: R1/R0 =3.3.

References:

35. A. Ishimaru, "Wave Propagation and Scattering in Random Media", IEEE Press, 1997.

36. G. Zaccanti, E. Battistelli, P. Bruscaglioni, Q. Wei, "Analytic relationships for the statistical moments of scattering point coordinates for photon migration in a scattering medium," *Pure Appl. Opt.* **3**, 897-905 (1994).

37. M. Born & E. Wolf, "Principles of Optics", Pergamon Press, 1987.

38. L. Wang, S. L. Jacques, L. Zheng, "MCML -- Monte Carlo modeling of light transport in multi-layered tissues," *Computer Methods & Programs in Biomedicine*, **47**, 131-46 (1995).

39. F. Martelli, S. Del Bianco, A. Ismaelli, G. Zaccanti, "Light Propagation through Biological Tissue and Other Diffusive Media: Theory, Solutions, and Software," *SPIE Press* (2009).

Post implant evaluation of implanted MPAs

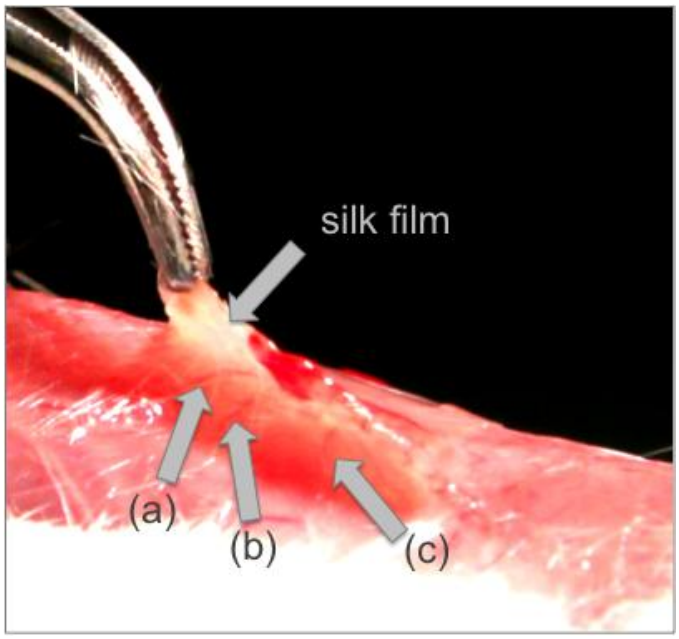

Figure S14. Post implant analysis of a silk film implanted in the dorsal region of a Balb/c mouse after 4 weeks of in-dwelling time. The arrows associated to (A), (B) and (C) provide some initial evidence of film reintegration and revascularization occurring around the implanted film.

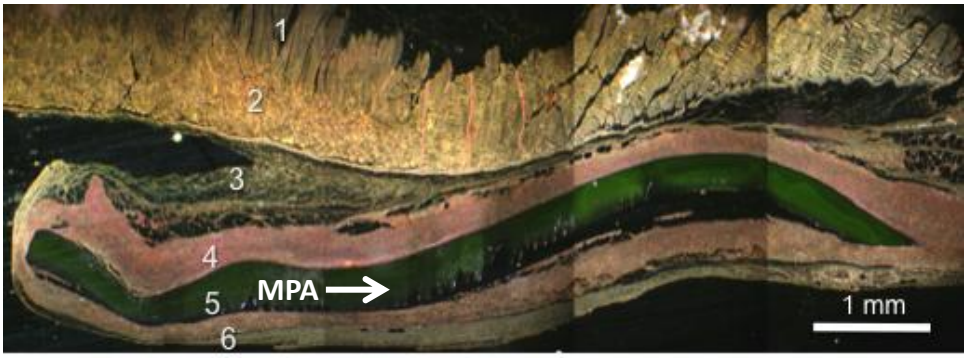

Figure S15. Full darkfield microscopy image of histological cross section of the 1 cm reflector implanted in the mouse (after 4 weeks of implantation time). Visible are the outer epidermis layer (1) and subcutaneous tissue (2), the silk film, the subcutaneous tissue (3, 4), and muscle tissue (6). The Subcutaneous tissue shows a thickening of the hypodermis directly under the implant (5) when compared to deeper hypodermis (3). The subcutaneous fat layer is unaffected (3).

In-vivo experiments: Reflectivity spectra of Au-NP doped plain silk film and micro-prism reflectors at 0 week and 2 weeks (N=3)

(a – Reflectivity spectra after implantation)

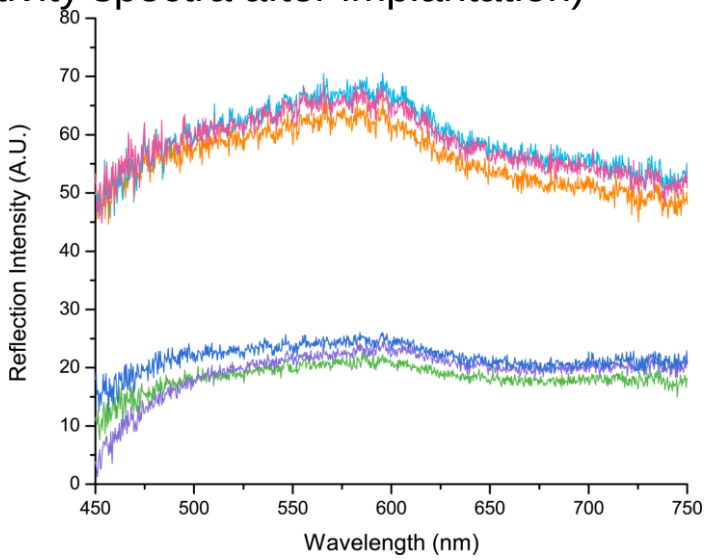

(b – Reflectivity spectra after 2 weeks)

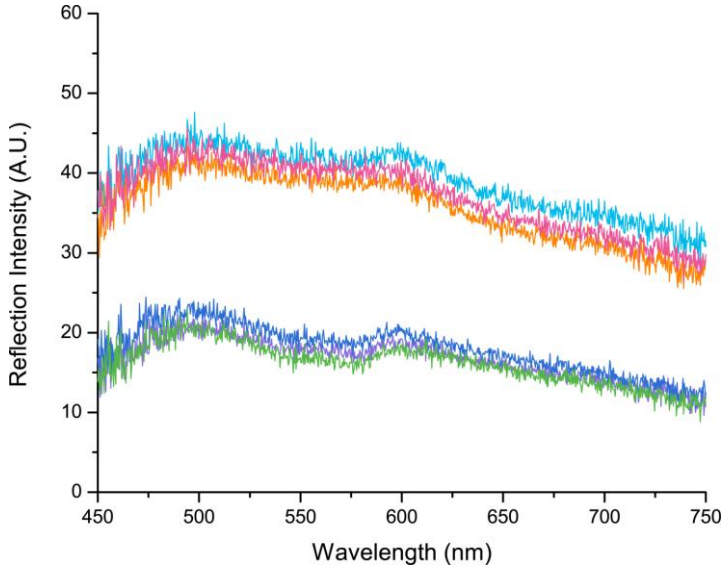

Figure S16. Reflectivity spectra of gold nanoparticle doped micro-prism film and plain silk at (A) 0 week and (B) 2 weeks (N=3). The optical fiber probe was placed against the mouse skin for the reflectivity measurements. The integration time was 25 millisecond with data average number = 10.

Spectral characterization of of Au-NP doped silk used for the preparation of the silk devices

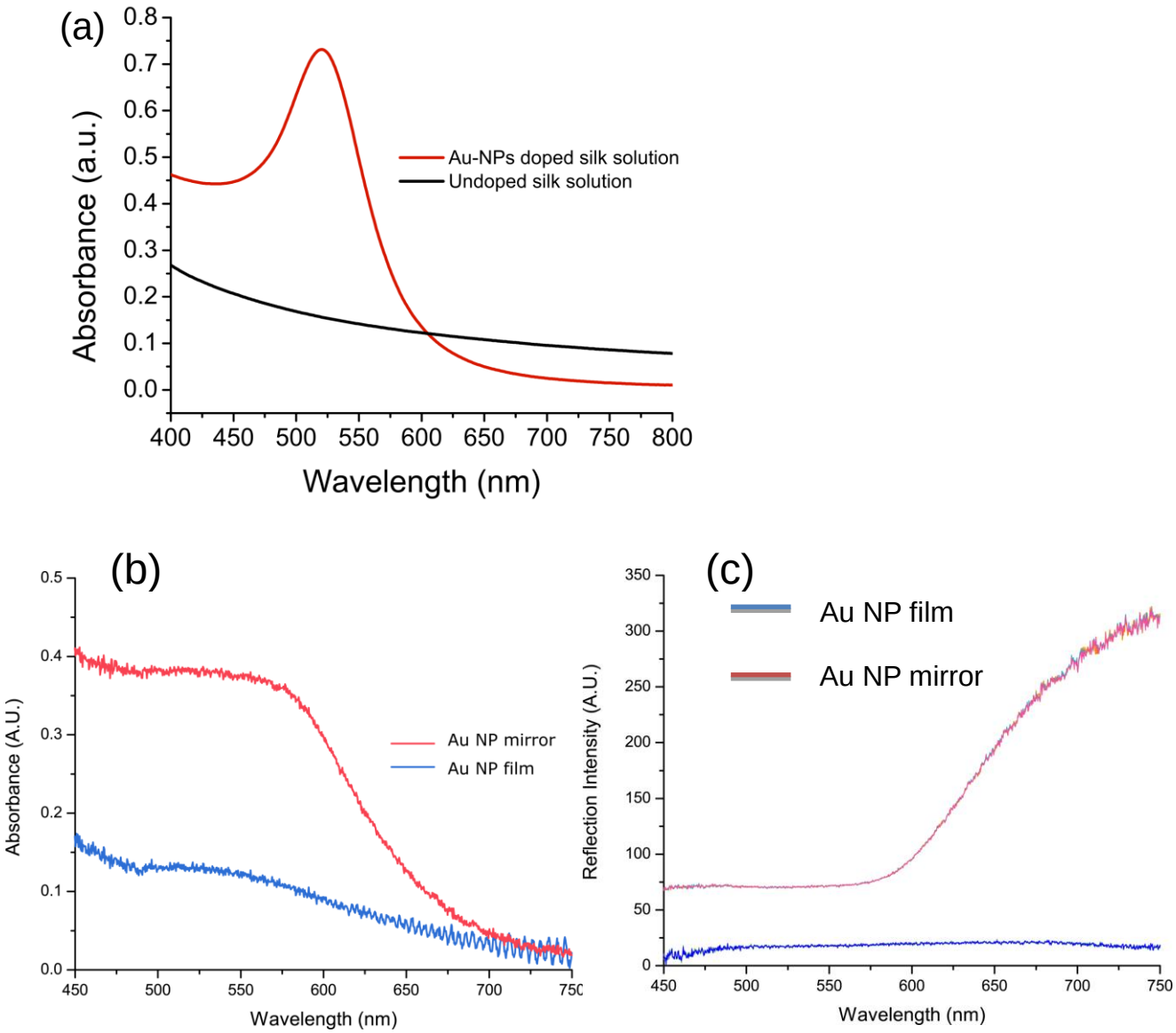

Figure S17. (A) Absorbance response of gold nanoparticles (Au-NPs) doped silk solution measured by UV-Vis spectrometer, showing a strong absorbance peak at ~ 532nm due to the plasmon resonant response of doped Au-NPs. Absorbance (B) and reflection (C) spectra of Au NPs doped silk film and reflector measured with Ocean Optics USB 2000 spectrometer.

Au-NP and bacterial lawn experiments

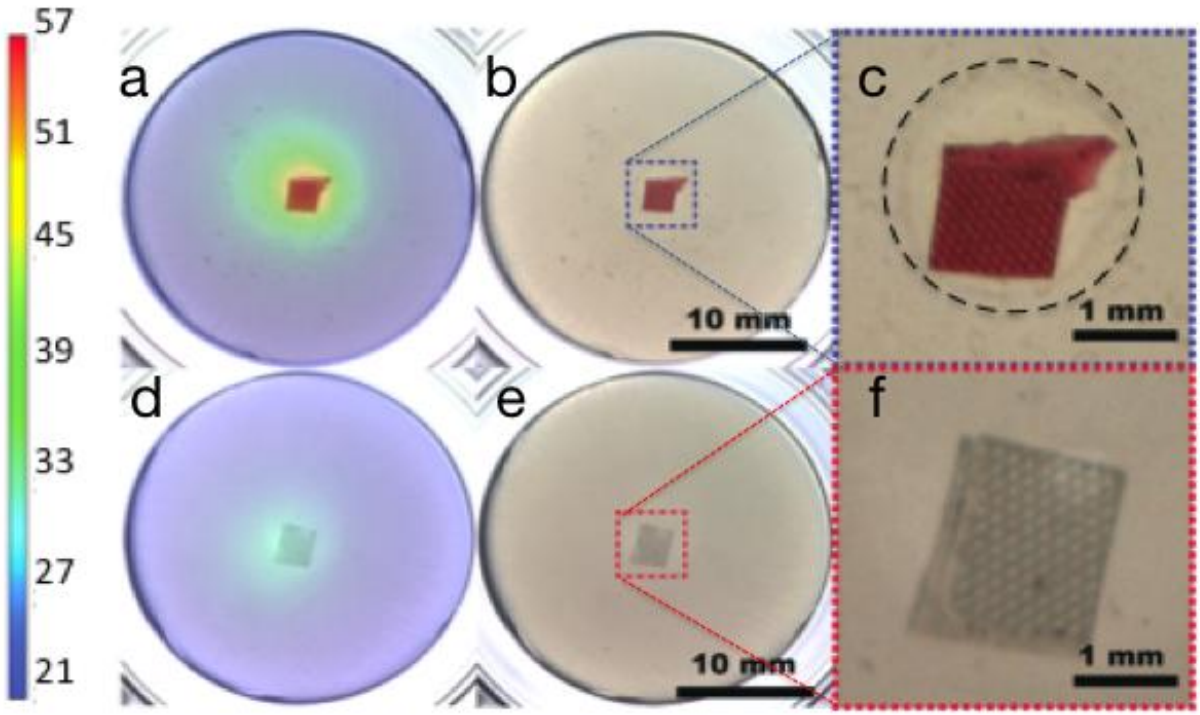

Figure S18 - The doped MPAs show enhanced absorption due to the Au-nanoparticle doping, as illustrated in (A). This is used to inhibit bacterial growth because of local heating caused by enhanced absorption as shown in (D) which illustrates a Au-NP-MPA and an undoped MPA embedded in E. Coli lawn. A zone of bacteria inhibition was observed after the laser illumination around the Au-NPs MPA, in contrast to the undoped silk MPA under the same λ=532 nm illumination conditions.

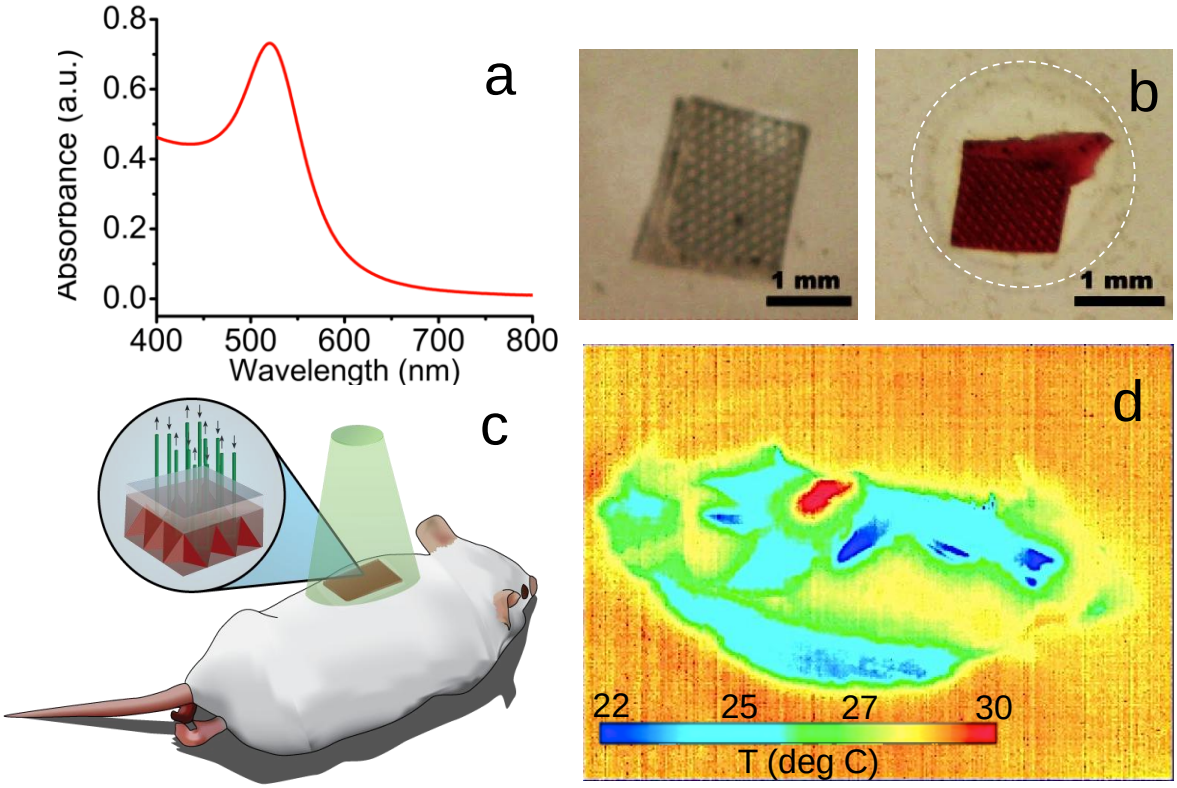

Figure S19 - The Au-NP-silk solution, which was used to cast MPAs, show enhanced absorption due to the Au-NP doping, as illustrated in (A). This is used to inhibit bacterial growth because of local heating caused by enhanced absorption as shown in (B) which illustrates a Au-NP-MPA and an undoped MPA embedded in E. Coli lawn. A zone of bacteria inhibition was observed after the laser illumination around the Au-NPs MPA, in contrast to the undoped silk MPA under the same λ=532 nm illumination conditions. The same concept is applied in vivo using the Au-NPs MPA as a light-activated thermal patch as illustrated in the scheme (C). The results are shown in (D). A temperature increase of ~ 5 °C at the implant site compared to surrounding tissues due to the Au-NPs absorption to green light is observed and recorded with a commercial IR camera (~ 5 cm in diameter and with a power of ~ 0.13 W/cm2).

Histological section of silk implants after 2 weeks implantation.

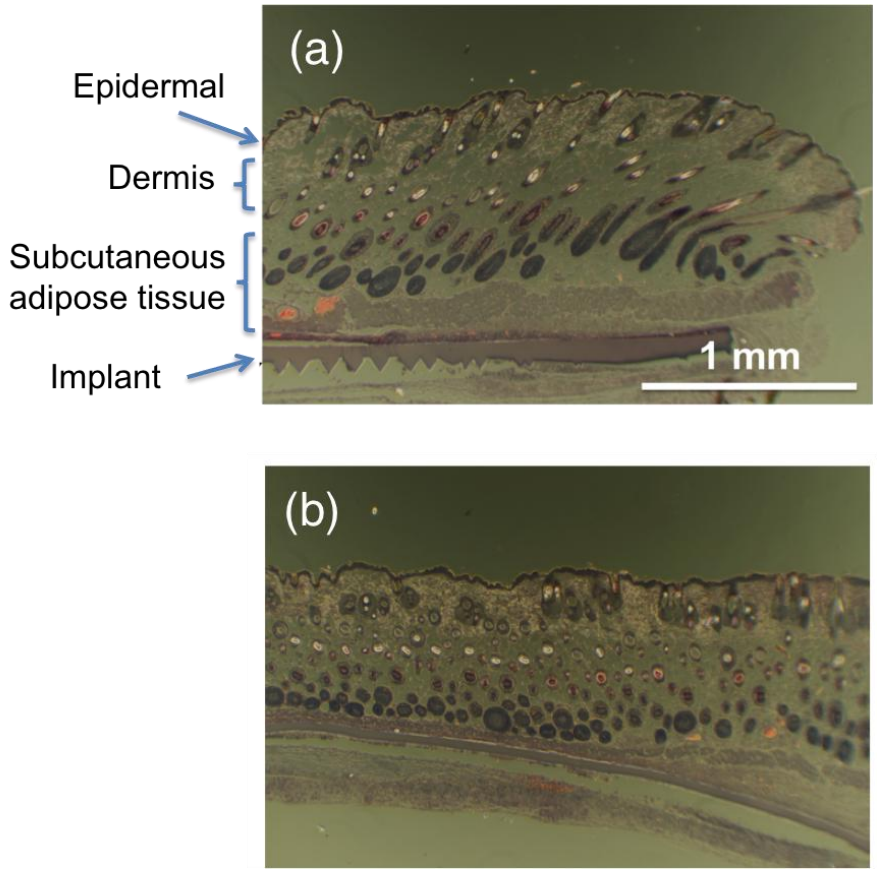

Figure S20. Microscopy images of histological cross section of (A) the implanted Au-NP reflector and (B) Au-NP silk film after 2 weeks of implantation time.

Release of Doxorubicin from Silk Films Relative to Proteolytic Degradation

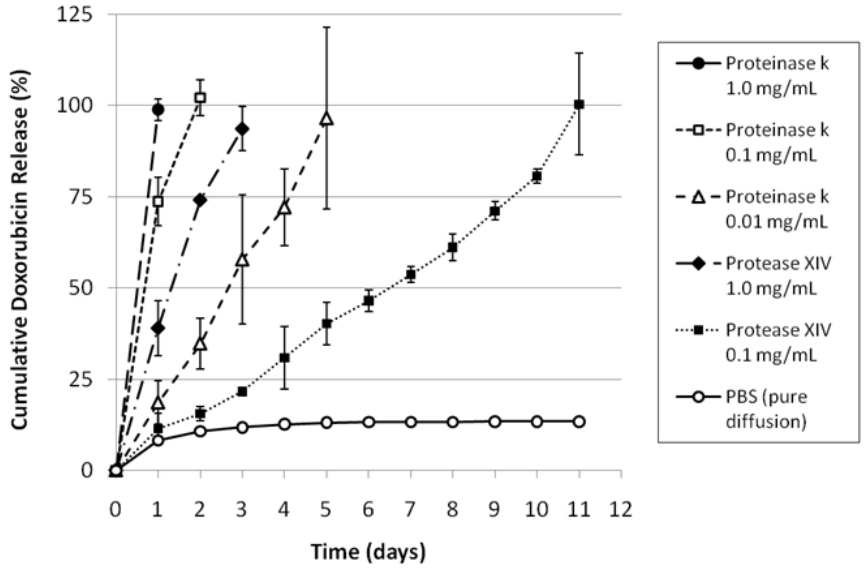

Figure S21. Cumulative doxorubicin release from reflector patterned silk films. N=3, error bars represent standard deviations (where error bars aren't shown, they fall into background). Doxorubicin quantified via absorbance at 495 nm (limit of detection = approx. 4 µg/mL)

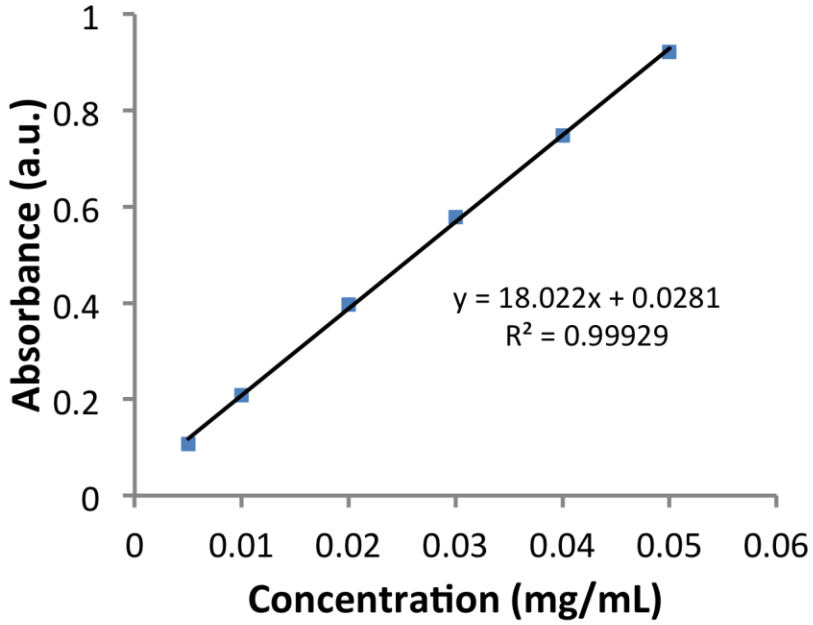

Figure S22. Doxorubicin concentration calibration curve by measuring the absorbance of the drug solution at 495 nm.

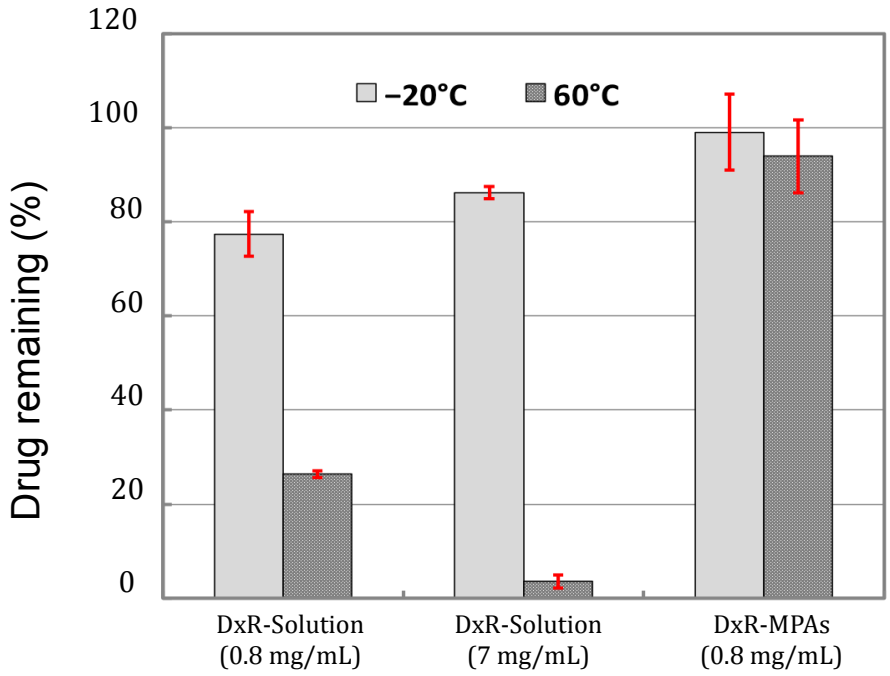

Figure S23. Doxorubicin in ultrapure water (two concentrations, 0.8 mg/mL and 7 mg/mL) and doxorubicin-loaded silk films were stored at -20°C and 60°C for 3 weeks. After 3 weeks, the silk films were degraded with 10 mg/mL proteinase k for 6 hours, and doxorubicin concentration for all samples was determined by comparing fluorescence to a standard curve of known concentrations (excitation = 430nm, emission = 550nm). Doxorubicin fluorescence decreases when stored in solution, while the fluorescence of the doxorubicin stored in silk films does not significantly decrease with the 80°C increase in storage temperature (N=3).

	Concentration (mg/mL)	**t_{50} (days)**
Proteinase k (approx. 30 units per mg)	1.0	0.51
	0.1	0.68
	0.01	2.66
Protease type XIV (approx. 3.5 units per mg)	1.0	1.31
	0.1	6.49

Table S1. Doxorubicin Increased proteolytic degradation (proteinase k degrades silk more aggressively than protease type XIV; increasing proteinase concentration increases rate of silk film degradation) decreases the time at which 50% of the total drug load is released (t_{50}). Films in PBS (no enzyme present, release is purely diffusional) release only 13.4% of the total drug load over 7 days, suggesting that for doxorubicin, drug release is predominantly degradation-mediated.

Doxorubicin Stabilization in Silk Films

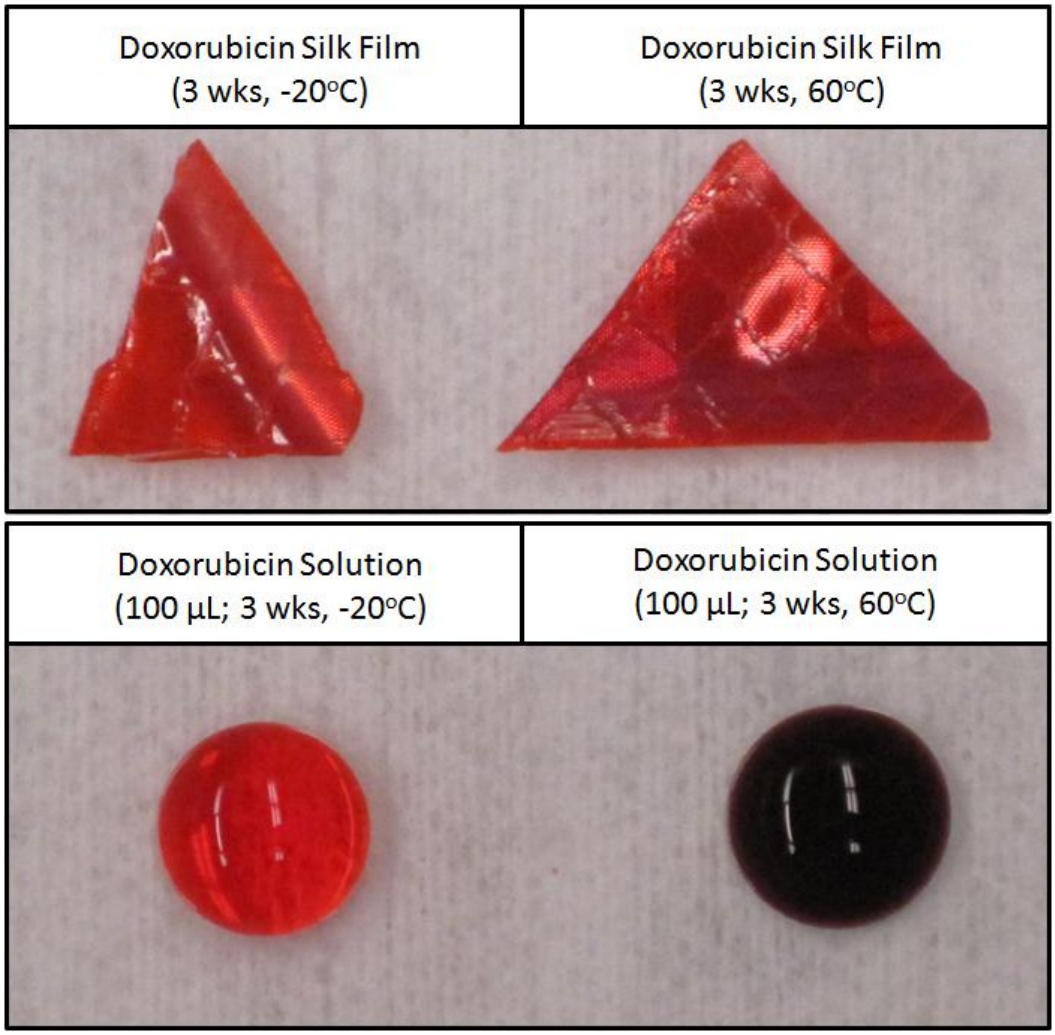

Figure S24. Images of doxorubicin in ultrapure water and doxorubicin-loaded silk micro-prism reflectors were stored at -20°C and 60°C for 3 weeks. Doxorubicin fluorescence decreases when stored in solution, while the fluorescence of the doxorubicin stored in silk films does not significantly decrease with the 80°C increase in storage temperature.

Materials and methods

Silk preparation

The purification of silk fibroin from Bombyx mori cocoons initially involves the removal of sericin, a water-soluble glycoprotein that binds fibroin filaments, by boiling the cocoons in a 0.02 M aqueous solution of sodium carbonate for 30 minutes. The resulting fibroin bundle is dried and then dissolved in a 9.3 M aqueous solution of lithium bromide at 60°C for four hours. The lithium bromide salt is then extracted through a water-based dialysis process over several days. The resulting solution is then centrifuged and filtered via syringe based micro-filtration (5 μm pore size, Millipore Inc., Bedford, MA) to remove any remaining particulates. This process enables the production of ~ 6.5-8% w/v silk fibroin solution with minimal contaminants and reduced scattering for optical applications.

Gold nanoparticle synthesis

Twenty ml of 1.0 mM gold chloride ($HAuCl_4$, Sigma-Aldrich) was added to a 100 ml round bottle, and boiled. Under rapid stirring, 2 ml of 1 % sodium citrate (Sigma-Aldrich) was added and further rapidly stirred for 15 min. After stirred for another 30 min, the solution was then gradually cooled to room temperature, and was filtered by 0.22 □m filter paper. This gives a gold nanoparticle solution with a concentration of ~3.5 nM and an average particle size of ~13 nm, which could be further concentrated to ~17.5 nM by being centrifuged for 20 min at 4^{o}C, with a RCF of 11930 g.

UV/VIS Spectroscopy

Absorption measurements of different samples were taken using a Lambda 35 UV/VIS Spectrometer (PerkineElmer, Waltham, MA). A gold nanoparticle doped silk solution (~ 7 nM Au-NPs solution: 6.5% w/v silk solution = 1:1 in volume) and a 6.5% w/v solution of undoped silk were measured with a bandwidth ranging from 400nm-800nm. Samples were compared to a reference blank of water.

Silk hydrogel preparation

The silk solution (~ 6.5% w/v) was then further diluted with deionized water down to 2 wt%, and 1 mL of 2 wt% solution was mixed for 7 minutes at 3,200 rpm using a vortexer (Fisher Scientific, Hampton, NH) to induce silk self-assembly and hydrogelation. Immediately after vortexing, while still in the liquid state, the addition of bacteria, Au-NP, and/or deionized water decreased the final silk concentration to ~1 wt%. This final composite solution was placed in a 37^{o}C incubator for 2 hours resulting in the transition to a gel state.

Laser spot size measurement

To profile the laser beam, the standard knife-edge technique was used. The incident beam was scanned with the edge of a razor blade, and the intensity of the light not blocked by the blade was measured with a power meter (PowerMax 500D, Molectron). From this, intensity vs. position graph was plotted for the beam profile. Lens adjustments were made to produce a Gaussian profile with a diameter of 3mm.

Thermal probing of bacteria loaded silk hydrogels

The bacteria loaded silk hydrogels, with and without gold nanoparticle doped silk mirrors, were probed via a green laser (Verdi V10, Coherent Inc.) operating at 532nm. The beam has a diameter of 3mm, and was directed onto the sample at an incident power of 500mW. Thermal images were taken using an IR camera (FLIR SC645, FLIR Inc.) from several angles after 10 minutes of treatment to determine the thermal response of the gels to the probe.

Bacteria culture

The bacteria strain used was *Escherichia coli* ATCC 25922 (American Type Culture Collection, Manassas, VA). Bacterial culture dishes, BD brand Luria-Bertani broth, Miller, BD brand Luria-Bertani agar, Miller, Tryptic Soy broth and Tryptic Soy agar were purchased from Fisher Scientific (Pittsburgh, PA). Luria Bertani (LB) and Tryptic Soy Broth were aliquoted into 100 mm diameter Fisherbrand cell culture plates (15-20 mL per plate). Lyophilized bacteria cultures were reconstituted and expanded according to instructions provided by ATCC. To test susceptibility, liquid cultures were grown for 18-24 hours to an optical density (OD_{600}) between 0.8 and 1 (corresponding to a viable count of approx. 10^7-10^8 CFU/mL). For the light-mediated bacteria inhibition experiments, bacteria with a concentration corresponding to an OD value of 0.8 were used.

***In vitro* zone of inhibition testing**

Antibacterial effect *in vitro* was estimated based on the principle of the Kirby-Bauer Susceptibility Test where antibacterial effect is assessed by comparing zones of clearance in bacterial lawns. Vortexed silk hydrogel and *E. Coli* overnight culture were mixed in a 1:1 volumetric ratio with the undoped and Au-NP doped micro-prism reflectors embedded in the center. The reflector-embeded silk hydrogels were then allowed to complete gelation (~ 2 hours). Hydrogels were then exposed to laser light of ~ 500 mW (with a beam size of ~ 3 mm) for 10 minutes and incubated 12 hours at 37^{o}C to allow lawn growth.

Release studies in proteinase k

To determine doxorubicin release from reflector patterned silk films the samples were immersed in 2 mL of 0.1 mg/mL proteinase type k (Sigma-Aldrich) solution in phosphate buffered saline (PBS). At selected time points, samples were removed from the proteinase containing buffer and the amount of released doxorubicin was determined by measuring the solutions absorbance at 495 nm using a GENESYS 10 UV-Vis scanning spectrophotometer (Thermo Scientific Inc.) and comparing measured values to a standard curve. In all cases PBS was used as a blank comparison solution (N=6).

Reflective losses measurements during enzyme degradation

Reflective measurements were taken using an Ocean Optics USB2000 Miniature Fiber Optic Spectrometer (Ocean Optics, Dunedin FL.) from 10 mm above the reflective surfaces. Black paper was used as the baseline dark background and an aluminum mirror and a white reflectance standard from Labsphere were used for the light background. The samples (from the DxR release experiments, N=6) were illuminated at normal incidence from a height of 10 mm. The mean value of remaining reflectivity (in ratio) was determined for each sample by comparing the mean values after water annealing and after proteinase treatment.

Animal experiments

Female Balb/c mice (6-8 weeks old) were anesthetized with an intraperitoneal injection of a ketamine/xylazine mix. Depth of anesthesia was monitored by palpebral and withdrawal reflexes to confirm that the animal had reached "stage 3" of anesthesia. Once the animal was lightly anesthetized, the back was shaved and cleaned at the incision site with 70 % ethanol, followed by a betadine surgical scrub. Once stage 3 was confirmed, a small longitudinal incision was made through the skin and the sterile implants (ethylene oxide sterilized) were inserted. The incision was closed with a Dexon 5-0 suture. The animal was monitored until ambulatory and given a dose of analgesia (Buprenorphine subcutaneously) as soon as surgery was completed.

Histology

To assess the safety of our heating procedure, we examined histological slices of tissues surrounding the implanted with reflectors. Samples were dehydrated through a series of graded alcohols, embedded in paraffin and sectioned at 10 μm thickness. Sections were stained with hematoxylin and eosin (H&E).